GEOMETRIC CHARACTERISTICS OF PASSIVE SCALAR INTERFACES FOR PLUMES IN TURBULENT BOUNDARY LAYERS

L.P. Dasi and D.R. Webster
School of Civil & Environmental Engineering
Georgia Institute of Technology
Atlanta, Georgia 30332-0355, USA
lakshmi.dasi@bme.gatech.edu, dwebster@ce.gatech.edu

ABSTRACT

The fractal geometry is quantified for concentration iso-surfaces of a high Schmidt number passive scalar field produced by an iso-kinetic source with an initial finite characteristic length scale released into the inertial layer of fully developed open channel flow turbulent boundary layers. The fractal dimension and other fractal measures of two-dimensional transects of the passive scalar iso-surfaces are found to be scale dependent. The fractal dimension is around 1.0 at the order of the Batchelor length scale and increases in a universal manner to reach a local maximum at a length scale around the Kolmogorov microscale. We introduce a new parameter called the coverage length underestimate, which reflects universal behavior in the viscous-convective regime and hence is a useful practical tool for many mixing applications. At larger scales (in the inertial-convective regime), the fractal measures are dependent on Reynolds number and concentration threshold of the iso-surfaces.

INTRODUCTION

Passive scalar fields in turbulent flows are highly convoluted structures that are continuously distorted by the fluctuating velocity field. These structures have been primarily studied from the classical turbulence theory point of view based on the concept of local isotropy and self-similar scalar variance cascade (Kolmogorov, 1941; Obukhov, 1949; Corrsin, 1951). This approach provides valuable results regarding the structure of scalar fields, but it lacks the ability to characterize the structure geometrically (Sreenivasan and Antonia, 1997; Shraiman and Siggia, 2000; Warhaft, 2000). Fractal geometry analysis allows geometric characterization and therefore has tremendous practical significance for understanding and predicting the dynamics of reactive and non-reactive turbulent mixing. Moreover, recent work has developed new fractal measures that have fundamental significance regarding the assumptions of the classical turbulence theory (Catrakis et al., 2002). Therefore, fractal geometry analysis is an important tool in the context of passive scalars in turbulent flows because it aids both fundamental understanding and practical application.

We report here the fractal geometry analysis of iso-surfaces of passive-scalar fields generated by an iso-kinetic release into turbulent boundary layers. Most previous studies have focused on the geometry of passive scalar (typically of a high Schmidt number) iso-surfaces for high-momentum round jet injection into a stagnant ambient fluid (Miller and Dimotakis, 1991; Catrakis and Dimotakis, 1996; Frederiksen et al., 1997; Catrakis et al., 2002). The choice of high-momentum jets is perhaps due to the practical relevance of mixing via jets, which is commonly employed by engineers when mechanical stirring is restricted. Also, the fractal characteristics for an iso-kinetic release have been previously studied in the far field of a high momentum jet (Villermaux and Innocenti, 1999). The current configuration has relevance for the analysis of plume mixing and dispersion characteristics of turbulent shear flows.

The objective of this study is to examine the scale distribution of two-dimensional transects of passive scalar iso-surfaces as a function of concentration threshold and Reynolds number. The scale distributions of iso-surfaces are analyzed via established fractal measures, such as the fractal dimension and coverage length. Additionally, a new parameter called the coverage length underestimate is presented.

EXPERIMENTAL PROCEDURE

Experiments were conducted to measure the fluctuating scalar field in equilibrium open-channel turbulent boundary layers for Reynolds number based on bulk velocity and flow depth of 5,000, 10,000, and 20,000 ($60 < Re_\lambda < 120$). Measurements were performed in a 1.07 m wide, 24.4 m long tilting flume for fully-developed, uniform flow conditions with a flow depth of 100 mm. Detailed velocity measurements obtained via Particle Tracking Velocimetry (PTV) are reported in Dasi (2004). The wall shear velocities, $u*$, were 3.25, 6.4 and 10.6 mm/s for the respective Reynolds number cases. The normalized mean velocity profiles coincided almost exactly with the viscous sublayer, buffer layer, and logarithmic layer. The Reynolds stress profiles also agreed very well with previous measurements of Tachie et al. (2003) and DNS results of Spalart (1988) for similar Re_θ.

The passive scalar field was generated by an iso-kinetic release (nozzle diameter of 4.7 mm) of the fluorescent dye Rhodamine 6G (Fig. 1). The center of the nozzle orifice was at an elevation of 50 mm above the flume bed. To minimize

the wake perturbation, the nozzle was custom-built with a streamlined fairing. The planar laser-induced fluorescence (PLIF) technique was used to collect long time records of the scalar field measured in a vertical plane parallel to the flow on the centerline of the plume. The laser sheet (created by sweeping the laser beam with a scanning mirror) caused the dye to fluoresce and a digital CCD camera (1396 × 1024 pixels, 12 bit/pixel) captured the emitted light over a 19 mm × 13 mm region (thus, the image resolution was 13 μm/pixel). In order to resolve the smallest relevant length scale, namely the Batchelor scale ($9\ \mu m < \eta_B < 24\ \mu m$ for the different Reynolds numbers), the laser beam passed through a beam expander and convex lens (1 m focal length), to give a $1/e^2$ diameter of 80 μm at the center of the image. Thus, the image plane was resolved at the order of the Batchelor scale and the sheet thickness was slightly larger. The laser beam swept through the flow very rapidly, essentially freezing the flow structure (less than 1% distortion error due to advection). A sample concentration field is shown in Fig. 2(a). The images were captured at a frame rate of 10 fps. For each data record, 12,000 consecutive images were captured. A careful calibration of the relationship of light intensity to the dye concentration was performed *in situ* for each individual pixel. All experimental procedures are described in detail in Dasi (2004).

Concentration iso-surfaces for defined concentration threshold levels were extracted for the 512×512 pixel array near the center of the image (shown in Fig. 2(a)), where the mean concentration gradient was approximately constant. Concentration iso-surfaces corresponding to four thresholds were extracted for each image. The threshold concentration, $\Theta_{th}(m)$, corresponded to m times the local standard deviation above the local mean (i.e. $\Theta_{th}(m) = \langle \Theta \rangle + m \langle \theta^2 \rangle^{1/2}$), where m was chosen to be 1, 3, 5, and 7. The range of useful concentration thresholds was bounded due to noise and limited sample size of the data sets. Due to the intermittent nature of the plume, the local mean concentration was orders of magnitude lower than the peak instantaneous concentration. The signal to noise ratio of intensities corresponding to concentrations lower than the local mean were poor and therefore limited the range of thresholds to be greater than the mean concentration. Also, for $m > 7$ only a small number of images contained iso-surface structure, which prevented statistically-converged measures.

Schuerg (2003) tested several iso-surface extraction methods and concluded that the boundary outline pixel approach is the superior method. A primary advantage of the boundary outline pixel method is that it eliminates the asymmetry between identifying "island" and "lakes" in the field. The methodology considered the concentration of a pixel (called the "center pixel") and compared it with the concentration of the eight neighboring pixels. If the concentration of the center pixel was greater than or equal to the threshold concentration, then the surrounding eight pixels were examined for threshold crossings. A neighboring pixel with a concentration below the threshold indicated a crossing between that pixel and the center pixel. A linear interpolation of the concentration between the two pixels was used to calculate the location of the crossing. The pixel closest to the crossing was flagged as a boundary outline pixel. If the location was exactly in the middle of the two pixels then both pixels were flagged as boundary outline pixels. This methodology was used for every pixel in each image to generate the iso-surface for the defined concentration threshold. The outcome was a binary

image consisting of the iso-surface (sample shown in Fig. 2(b)).

Coverage statistics of the iso-surface were based on the coverage count generated by the box-counting algorithm. In the box-counting algorithm, the maximum image area was termed as the bounding box of size δ_b (= 512 pixels for the present study). The bounding box was subdivided into $N_{2,tot}(\lambda)$ squares of area λ^2, and the number of squares that contain any part of the iso-surface was counted as $N_2(\lambda)$. The subscript 2 stands for the embedding dimension, $d = 2$ for our planar measurements. The coverage count was generated for the range $0 < \lambda < \delta_b$ at logarithmically equally-spaced discrete values of λ. The coverage statistics were estimated from the discrete coverage count $N_2(\lambda)$ generated at 10 levels of λ. The 10 levels of λ, denoted by λ_s, correspond to 512, 256, 128, 64, 32, 16, 8, 4, 2 and 1 pixels for $s = 1,2,...,10$. Following the recommendation of Miller and Dimotakis (1991), the starting position of the subdivision was shifted to eight starting locations (in each coordinate direction). Thus, for each box size, λ, we shifted the grid to 8×8 = 64 different locations. For the smallest scale of one pixel, only one position was possible. For the second-smallest subdividing box, there were 2×2 = 4 possible shifting positions, and so on. Of course, it does not make sense to shift the grid for the largest length scale. Some boxes shifted past the boundaries of the image. In such circumstances, we artificially connected the left image boundary to the right one, and the upper image boundary to the lower one. As discussed in the next section, other fractal measures were calculated based on the coverage count results. The results were ensemble-averaged over the full record of images.

Schuerg (2003) validated the coverage statistics calculation algorithm by evaluating the performance when applied to deterministic self-similar fractal objects of known theoretical dimension. Based on Koch curves given by Mandelbrot (1982), five deterministic fractals with the dimensions D = 1.1046, 1.2553, 1.4466, 1.6131, and 1.7604 were developed and analyzed. In each test the algorithm satisfactory produced the expected coverage statistics.

RESULTS AND DISCUSSION

The coverage count, at a given scale, λ, is the number of boxes of size λ in the grid that contain any part of the scalar iso-surface within the bounding box. There are a number of other measures based on the coverage count that yield a comprehensive description of the fractal geometry of the iso-surfaces. These measures are collectively called the coverage statistics. In general, the coverage statistics of a set focus on the space filling properties and scale distributions of the set. Catrakis and Bond (2000) provide a valuable overview of the coverage statistics.

Figure 3 shows the coverage count for the four threshold levels. The coverage count decreases with λ and threshold level. The decrease with respect to threshold level is consistent with Miller and Dimotakis (1991) for passive scalar mixing in a turbulent jet. Also, the coverage count at $\lambda = \delta_b$ is not necessarily unity and decreases with increasing threshold due to the presence of empty bounding boxes attributed to the highly intermittent scalar field. The negative slope of the curves decreases in magnitude with threshold

level, for scales greater than the Kolmogorov scale (at $\log_{10}(\lambda/\delta_b) = -1.2$) for the three higher thresholds.

The coverage dimension is defined as the negative of the logarithmic derivative of the coverage count of the surface. The coverage dimension or box-counting dimension, $D_d(\lambda)$, is thus given by:

$$D_d(\lambda) = -\frac{d \log N_d(\lambda)}{d \log \lambda} \qquad (1)$$

The term fractal dimension is often used synonymously with coverage dimension. Although the coverage dimension is not equal to the more rigorous measure (namely the Hausdorff dimension) even for simple deterministic self-similar fractals, it successfully captures most characteristics of fractal surfaces.

Figure 4 shows the variation of the coverage dimension with respect to concentration threshold. The coverage dimension approaches the topological dimension, $d_t = 1$, as $\lambda \to \eta_B$ reflecting the fact that iso-surfaces are ultimately smooth curves at scales below the order of the Batchelor scale. From the figure, the coverage dimension is clearly scale dependent, irrespective of threshold, in agreement with the observations of Catrakis and Dimotakis (1996) for high momentum jets. The coverage dimension for all thresholds increases with scale in the viscous-convective range $-2.7 < \log_{10}(\lambda/\delta_b) < -1.2$, indicating that the convolution of the iso-surfaces appears to be more space filling with increasing scale. Also, the coverage dimension in the viscous-convective range is less sensitive to variations in the concentration threshold. The coverage dimension appears to be the same for the three higher concentration thresholds, while that of the lowest threshold shows a mildly elevated coverage dimension which may be attributed to mediocre signal to noise ratio for the given threshold.

The curves at scales greater than the Kolmogorov length scale are sensitive to variations in the concentration threshold where coverage dimension appears to decrease with scale size for the higher thresholds. The decrease in coverage dimension is due to the fact that at scales larger than the Kolmogorov scale, the scalar blobs are often completely inside the λ-sized boxes thereby appearing as a collection of spots. This, combined with the presence of empty boxes in the ensemble, explains why the coverage dimension falls below $d_t = 1$. Unlike the previous observations in jet flows, the iso-surfaces appear more and more "spotty" ($D_2 < 1$) as the size of the boxes increases. Note that for the lowest concentration threshold the coverage dimension continues to increase with scale size in the inertial-convective regime. This variation is not an artifact of noise but instead indicates that the size of the scalar iso-surfaces at low thresholds increases faster than the size of iso-surfaces of higher thresholds. This is true because these iso-surfaces correspond to the far edges of the scalar blobs where molecular diffusion is expanding the iso-surface.

Figure 5 shows the variation of coverage dimension with Reynolds number. In the viscous-convective regime the coverage dimension appears to be independent of Reynolds number except for the lowest Reynolds number where the curve is slightly flatter than those for higher Reynolds numbers. It has also been shown that the coverage dimension is independent of the initial length scale (i.e. nozzle size) at which the scalar is introduced into the flow (Dasi, 2004). It can be concluded that the coverage dimension in the viscous-

convective range behaves in a universal manner for high Reynolds numbers. In the inertial-convective range, the coverage dimension for the two highest Reynolds numbers are fairly coincident for each threshold level. The coverage dimension for the lowest Reynolds number is significantly lower in this range. This Reynolds number dependence may be explained from fact that the intermittency factor increases with Reynolds number (Dasi, 2004). This implies that the scalar field does not appear as sparse as for lower Reynolds number, thereby increasing the coverage dimension. Note that the coverage dimension remains below 1 in the inertial-convective range for the range of Reynolds number. For higher Reynolds number, the coverage dimension in this range may exceed 1, which would indicate that the iso-surfaces, although sparse, have smoother large scale structures.

The coverage length, $L_d(\lambda)$, measures the total length of the scalar iso-surface in the bounding box using the ruler of size λ. For the present case with $d = 2$, this measure corresponds to the length of the scalar iso-surface, which can be thought of as an interface boundary. For higher dimension, it corresponds to interface area, volume, and so on, per bounding box. This measure is estimated as:

$$L_d(\lambda) = \lambda^{d_t} N_d(\lambda) \qquad (2)$$

where d_t is the topological dimension of the set and is equal to 1 for our measurements. Note that $L_d(\lambda)$ generally increases with decreasing λ and tends to the total coverage length, $L_{d,tot}$, as $\lambda \to 0$. For classical fractals, the total coverage length is infinity due to self-similarity at arbitrarily small scales. We represent this measure as the coverage length per unit bounding box area.

Figure 6 shows the total coverage length in millimeters per square millimeter of the measurement region for different concentration thresholds. In the viscous-convective range, the coverage length decreases with increasing scale and the curves corresponding to different thresholds appear nearly parallel. Above the Kolmogorov length scale, there is a change in the trend dependent on the threshold. For the lowest threshold the coverage length continues to decrease, whereas for the other thresholds the curve attains a local minima followed by an increase in coverage length. The increase with increasing scale size is possible as the coverage dimension at these scales falls below unity. Overall, the coverage length decreases with increasing threshold. This decrease with increasing threshold can be explained in analogy to the contour lines of "tapered peaks or hills" of concentration. Increasing the threshold moves the contour up the hill while reducing the length of the contour. As $\lambda \to 0$, the coverage length of each curve approaches the true length of the iso-surfaces, while the lengths measured at higher scales may be interpreted as artifacts of lower resolution.

Schuerg (2003) introduced the coverage length underestimate, $\langle L_{2,u}(\lambda/\delta_b) \rangle$, defined as:

$$\langle L_{2,u}(\lambda/\delta_b) \rangle = \frac{\langle L_{2,tot} \rangle}{\langle L_2(\lambda/\delta_b) \rangle} \qquad (3)$$

The coverage length underestimate is essentially the ratio of the total iso-surface length to the length measured at larger scale size. This measure is useful because the coverage length

underestimate shows universal characteristics similar to the coverage dimension (discussed below).

It can be shown that a universal variation of the fractal dimension in the viscous-convective regime corresponds with universal behavior of the coverage length underestimate (Dasi, 2004):

$$L_{d,u}(\lambda) = \exp\left(\int_0^\lambda \frac{1}{\tilde{\lambda}}\left(D_d(\tilde{\lambda}) - d_t\right)d\tilde{\lambda}\right) \qquad (4)$$

Consequently, one may estimate the true interfacial length based on the universal variation of the fractal dimension in the viscous-convective regime.

Figure 7 shows the coverage length underestimate for the four threshold levels. The figure shows that the true coverage length is about 150-200% greater than that measured at the resolution of the Kolmogorov length scale. The coverage length underestimate is largely independent of the threshold level in the viscous-convective range. Note that the curve corresponding to the lowest threshold shows elevated coverage length underestimate in this regime (similar to the elevated coverage dimension in Fig. 4). Figure 8 shows the coverage length underestimate for different Reynolds numbers. The figure indicates that the coverage length underestimate is independent of the Reynolds number in the viscous-convective regime. In the inertial-convective range, the coverage length underestimate increases with Reynolds number.

CONCLUSION

This paper presents an analysis of the field generated by an iso-kinetic release of a high Schmidt number passive scalar into a turbulent boundary layer. In particular, the paper presents an analysis of the local-structure from an applied view point via the tools of fractal geometry. The passive scalar iso-surfaces were analyzed by the box-counting algorithm to generate various scale-dependent coverage statistics of the iso-surfaces including the fractal dimension. The raw iso-surface images were qualitatively different from those reported in the archival literature for the case of scalar fields generated via high-momentum jets. Here, the scalar field was highly intermittent and consisted of sparse filaments in the measurement plane. The fractal measures of the iso-surfaces were found to be scale dependent with Level 3 complexity.

The fractal dimension (of two-dimensional transects of the passive scalar iso-surfaces) was observed to be close to the topological dimension of 1.0 at scales near the Batchelor scale. The fractal dimension increased with increasing scale, which indicates that the interfaces were smooth at the smallest scale. For the higher concentration thresholds the fractal dimension reached a maximum around the Kolmogorov length scale indicating maximum convolution at this scale. Fractal dimension values below the topological dimension were observed for higher thresholds due to the sparseness of the filaments. The fractal dimension was sensitive to all experimental parameters. However, in the viscous-convective regime the fractal dimension appeared to follow a universal behavior. The fractal dimension at larger scales decreased with increasing concentration threshold, and it increased, to some degree, with increasing Reynolds number.

Other fractal measures collectively known as the coverage statistics were also examined. Most importantly, a new measure, namely the coverage length underestimate, was calculated for the passive scalar iso-surfaces. The coverage length underestimate is a useful measure for modeling because it provides information for the true interfacial length given a coarse observation or simulation of the passive scalar field. Consequently, one may estimate the true interfacial length based on the variation of the fractal dimension in the viscous-convective regime.

REFERENCES

Catrakis, H.J., Aguirre, R.C., and Ruiz-Plancarte, J., 2002, "Area-Volume Properties of Fluid Interfaces in Turbulence: Scale-Local Self-Similarity and Cumulative Scale Dependence", *J. Fluid Mech.*, Vol. 462, pp. 245-254.

Catrakis, H.J., and Bond, C.L., 2000, "Scale Distributions of Fluid Interfaces in Turbulence", *Phys. Fluids*, Vol. 12, pp. 2295-2301.

Catrakis, H.J., and Dimotakis, P.E., 1996, "Mixing in Turbulent Jets: Scalar Measures and Isosurface Geometry", *J. Fluid Mech.*, Vol. 317, pp. 369-406.

Corrsin, S., 1951, "On the Spectrum of Isotropic Temperature Fluctuations in an Isotropic Turbulence", *J. Applied Physics*, Vol. 22, pp. 469-473.

Dasi, L.P., 2004, "The Small-Scale Structure of Passive Scalar Mixing in Turbulent Boundary Layers", Ph.D. Thesis, Georgia Institute of Technology, Atlanta, GA.

Frederiksen, R.D., Dahm, W.J.A., and Dowling, D.R., 1997, "Experimental Assessment of Fractal Scale Similarity in Turbulent Flows. Part 2. Higher-Dimensional Intersections and Non-Fractal Inclusions", *J. Fluid Mech.*, Vol. 338, pp. 89-126.

Kolmogorov, A.N., 1941, "The Local Structure of Turbulence in Incompressible Viscous Fluid for Very Large Reynolds Numbers", *Dolk. Akad. Nauk SSSR*, Vol. 30, pp. 301.

Mandelbrot, B.B., 1982, *The fractal geometry of nature*, W.H. Freeman, New York.

Miller, P.L., and Dimotakis, P.E., 1991, "Reynolds Number Dependence of Scalar Fluctuations in a High Schmidt Number Turbulent Jet", *Phys. Fluids A*, Vol. 3, pp. 168-177.

Obukhov, A.M., 1949, "The Structure of the Temperature Field in a Turbulent Stream", *Izvestiya Akademii Nauk SSSR, Geogr. and Geophys. Ser.*, Vol. 13, pp. 58-69.

Schuerg, F., 2003, "Fractal Geometry of Iso-Surfaces of a Passive Scalar in a Turbulent Boundary Layer", M.S. Thesis, Georgia Institute of Technology, Atlanta, GA.

Shraiman, B.I., and Siggia, E.D., 2000, "Scalar Turbulence", *Nature*, Vol. 405, pp. 639-646.

Spalart, P.R., 1988, "Direct Simulation of a Turbulent Boundary-Layer up to $Re_\theta = 1410$," *J. Fluid Mech.*, Vol. 187, pp. 61-98.

Sreenivasan, K.R., and Antonia, R.A., 1997, "The Phenomenology of Small-Scale Turbulence", *Annu. Rev. Fluid Mech.*, Vol. 29, pp. 435-472.

Tachie, M.F., Balachandar, R. and Bergstrom, D.J., 2003, "Low Reynolds Number Effects in Open-Channel Turbulent Boundary Layers", *Exp. Fluids*, Vol. 34, pp. 616-624.

Villermaux, E., and Innocenti, C., 1999, "On the Geometry of Turbulent Mixing", *J. Fluid Mech.*, Vol. 393, pp. 123-147.

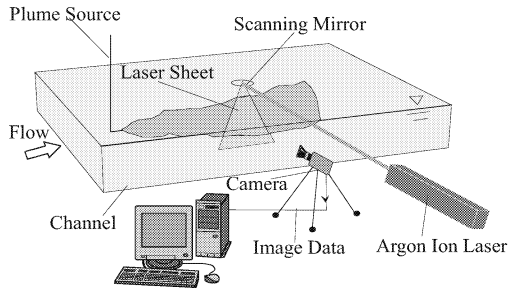Warhaft, Z., 2000, "Passive Scalars in Turbulent Flows", *Annu. Rev. Fluid Mech.*, Vol. 32, pp. 203-240.

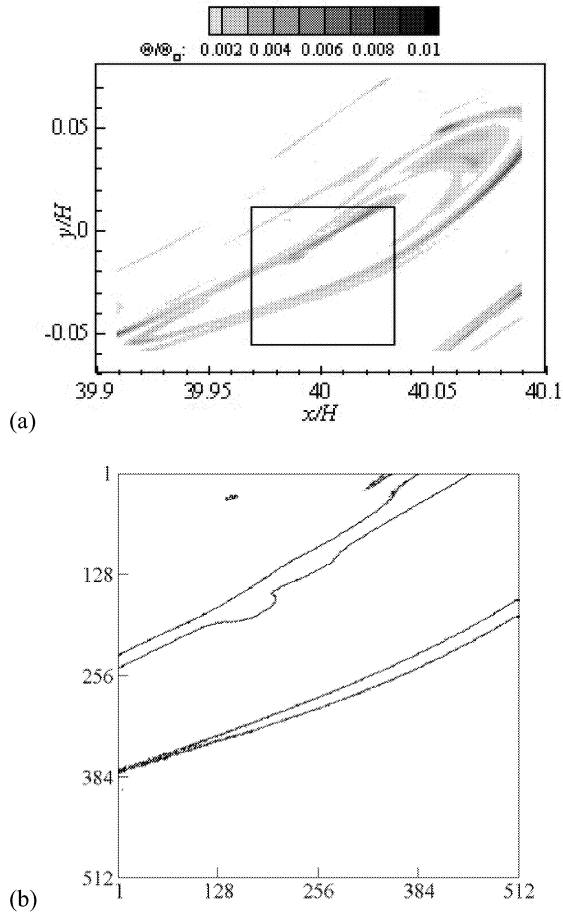Figure 1 : Schematic of the experiment setup.

(a)

(b)

Figure 2 : (a) Sample concentration field, and (b) corresponding boundary outline image for m = 1. Data shown for x = 4 m, Re = 10,000 and D = 4.7 mm.
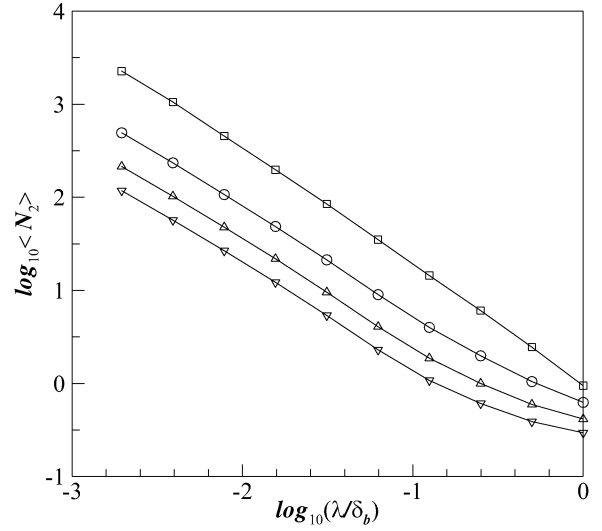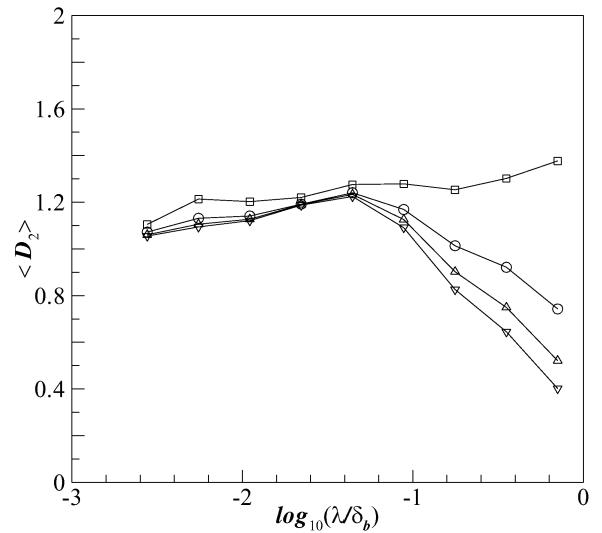

Figure 3 : Coverage count as a function of concentration threshold. Data plotted versus normalized scale, λ / δ_b , for the passive scalar iso-surface at a concentration m times the local standard deviation above the local mean, for m = 1 ($\square$), 3 ($\circ$), 5 ($\triangle$), and 7 ($\triangledown$), at x = 4 m; for D = 4.7 mm and Re = 10,000.

Figure 4 : Coverage dimension as a function of concentration threshold. Data plotted versus normalized scale, λ / δ_b , for the passive scalar iso-surface at a concentration m times the local standard deviation above the local mean, for m = 1 ($\square$), 3 ($\circ$), 5 ($\triangle$), and 7 ($\triangledown$), at x = 4 m; for D = 4.7 mm and Re = 10,000.
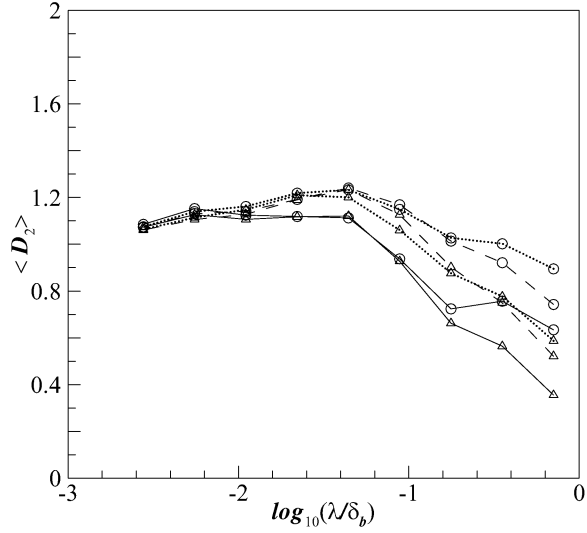
Figure 5 : Coverage dimension as a function of Reynolds number. Data plotted versus normalized scale, λ / δ_b, for the passive scalar iso-surface at a concentration m times the local standard deviation above the local mean, for m = 3 (○) and 5 (△), at x = 4 m; for D = 4.7 mm and Re = 5000 (——), 10,000 (– – –), and 20,000 (••••••••).

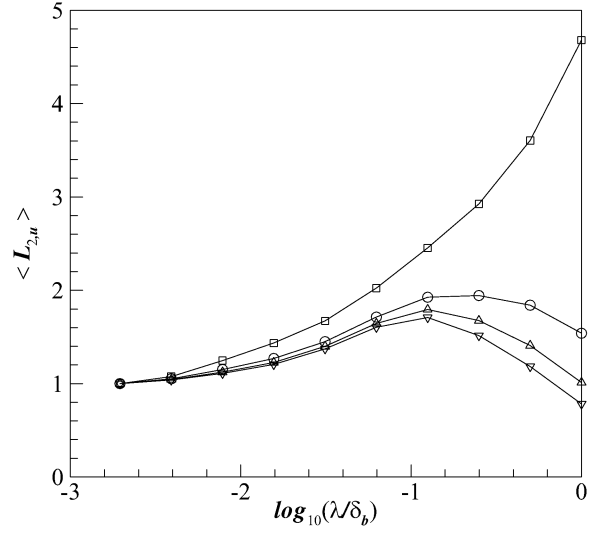Figure 7 : Coverage length underestimate as a function of concentration threshold. Data plotted versus normalized scale, λ / δ_b, for the passive scalar iso-surface at a concentration m times the local standard deviation above the local mean, for m = 1 (□), 3 (○), 5 (△), and 7 (▽), at x = 4 m; for D = 4.7 mm and Re = 10,000.
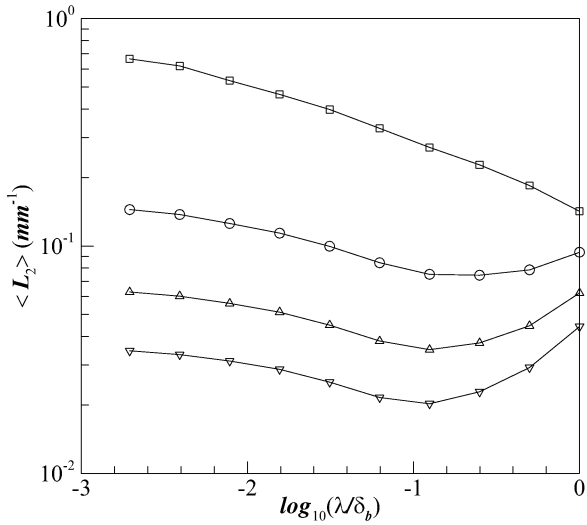

Figure 6 : Coverage length as a function of concentration threshold. Data plotted versus normalized scale, λ / δ_b, for the passive scalar iso-surface at a concentration m times the local standard deviation above the local mean, for m = 1 (□), 3 (○), 5 (△), and 7 (▽), at x = 4 m; for D = 4.7 mm and Re = 10,000.
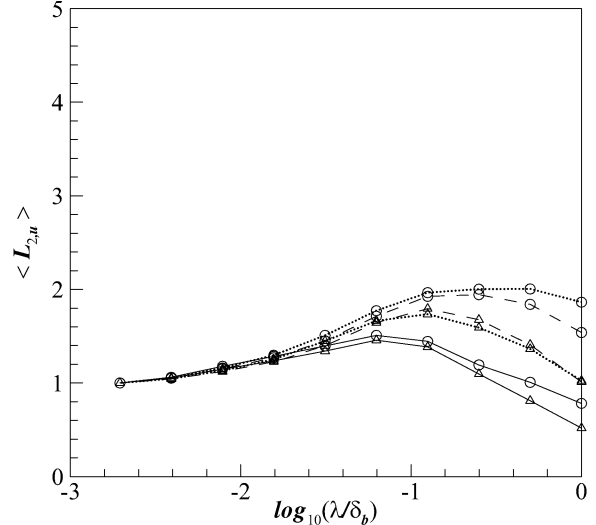

Figure 8 : Coverage length underestimate as a function of Reynolds number. Data plotted versus normalized scale, λ / δ_b, for the passive scalar iso-surface at a concentration m times the local standard deviation above the local mean, for m = 3 (○) and 5 (△), at x = 4 m; for D = 4.7 mm and Re = 5000 (——), 10,000 (– – –), and 20,000 (••••••••).